Continuous-control-set Model Predictive Current Control of Asymmetrical Six-phase Drives Considering System Non-idealities

Chee Shen Lim, *Senior Member*, *IEEE*, Sze Sing Lee, *Senior Member*, *IEEE*, Emil Levi, *Fellow, IEEE*

Abstract—Finite-control-set model predictive control (FCS-MPC) of multiphase (*n*-phase, *n* is assumed to be an odd number for simplicity) drives is challenging because of the large number of actual/virtual voltage vectors and the need for current control in (*n*-1)/2 sub-spaces (or planes; multi-plane current control). Any sub-optimal design (poor or no current control in some of the (*n*-1)/2 planes) may result in high individual plane current ripples, due to the low reactance. This work therefore investigates continuous-control-set (CCS) MPC for constant switching frequency multiphase motor drives as another alternative. The high-bandwidth CCS-MPC is designed to accurately account for system non-idealities, namely digital control and pulse width modulation delays, inverter dead time, and measurement noise. It will be shown that the CCS-MPC has the advantages of full voltage vector space access, regular switching characteristic, and improved cycle-by-cycle tracking control, while maintaining some of the known advantages of the FCS-MPC, e.g., intuitive cost function design, model-based control, and fast dynamics. The proposed control scheme is benchmarked experimentally against the classical, proportional-integral-based, field-oriented control in conjunction with an asymmetrical six-phase induction motor drive.

Index Terms—Multiphase drives, model predictive control, finite control set, continuous control set.

I. INTRODUCTION

Model predictive control (MPC) has been studied extensively in conjunction with multiphase drives in the last decade [1]–[3]. One of the earlier problems encountered by the modulator-free FCS-MPC is the high number of switching states in a multiphase (more than three phases) system, making it computationally prohibitive for higher phase orders (even more so with multilevel inverters). The heaviness of the computational problem can be alleviated by using reduced sets of switching states without worsening the machine current ripple, compared to the use of the full set counterpart [4]. Nevertheless, earlier works, e.g. [4], [5],

C. S. Lim is with the School of Advanced Technology, Xi'an Jiaotong-Liverpool University, Suzhou Industrial Park, Suzhou 215123, China (e-mail: cheeshen.lim@xjtlu.edu.cn)

S. S. Lee is with the Newcastle University in Singapore, Singapore 567739, Singapore (e-mail: ss.lee@ieee.org).

E. Levi is with the Faculty of Engineering and Technology, Liverpool John Moores University, Liverpool L3 3AF, U.K. (e-mail: E.Levi@ljmu.ac.uk).

showed that modulator-free MPC with actual voltage vectors (VVs) would suffer from high sub-space (i.e. plane) current ripples in multiphase motor drives due to the low sub-space reactance. This phenomenon is due the controller's inability to eliminate cycle-by-cycle tracking cost function errors [4], [5]. It is worth noting that, as far as MPC in power electronics is concerned, this feature relates to several factors, e.g., cost function design, modulator's switching pattern, parameter accuracy, that affect the steady-state control performance.

Earlier attempts to improve the steady-state current ripple performance centered on the concept of zeroing the sub-space voltage(s), leading to single-plane control strategies. This includes the techniques with predefined virtual VVs [6] and individual cost function based modulation of large-zero [7] and large-medium VVs [8], with manually defined switching patterns. The deadbeat mechanism that first calculates the primary (flux-torque producing) plane's reference voltage vector was exploited in [9], [10], followed by identifying the best VV from the pre-defined set of primary plane virtual VVs. The effect of further modulating the best virtual VV with a zero vector was also studied in [10]. Solutions in [6]–[10] are characterized with the problem of limited trajectory of the synthesizable voltage vectors because only limited points or lines are accessible by the predictive control. This problem is solved to some extent in [11], [12]. A three-stage optimization in which two best virtual VVs are first identified is presented in [11], followed by identifying the best discrete duty ratios. Modulation with the two best primary virtual VVs and a zero vector is investigated in [12]. [13] presented a flux-torque deadbeat based geometric calculation that computes the duty ratio of the second VV (zero or virtual). With zero second-plane voltage, the low-frequency sub-space voltages/currents, which can appear due to a drive's non-idealities (e.g. inverter dead-time effect [4], [14], machine asymmetries, flux linkage harmonics in permanent magnet machines and in machines with trapezoidal back-EMF [15]), can no longer be controlled.

As far as full current control (i.e. current control in all planes), including primary plane's flux/torque control, is concerned, there are in general two groups of solutions, characterized by their accessibility to the multidimensional VV space: partial or full VV space access. Partial space access means that limited discrete actual [4], [5] or virtual VVs, being points or lying along two-dimensional lines in the vector space, are deployable by the predictive control. One such solution, based on three-stage enumeration where the best couple of actual VVs and the best discrete duty ratios are computed, is proposed in [16]. On the other hand, [16] uses the voltage

reference computed from deadbeat torque-flux control to identify the nearest three actual VVs (additionally constrained to those aligned). Both [16], [17] have limited voltage space access. Despite the simpler sub-space-only cost function, the cycle-to-cycle cost error is usually not zero. The same problem can be found in the two-plane current control scheme [15] that exploits deadbeat current principle for identifying the nearest virtual VV in each sub-space. Full VV space access is available in the solution of [18], which investigated a predictive current control technique that deploys a two-stage-optimized, dual-pair modulated virtual VVs tracking individual sub-space currents, while zeroing the voltage in the other(s). The continuous duty ratio is found through an analytical solution and is limited to avoid overmodulation.

All advanced MPC schemes of multiphase drives reported to date have in common enumerating through and/or identification of a subset of actual/virtual VVs, followed by duty cycle(s) estimation. This design methodology typically faces the following challenges:

(i) Predictive control algorithm is complex in drives with multilevel inverters. An example can be seen in a five-phase three-level system [18] where cost evaluation must be reduced, e.g. from 81 to 4 times, to make the algorithm feasible in practice. The size of look-up table may also be too large, leading to implementation concerns.

(ii) An elaborate predictive algorithm, e.g. multistage optimization [17], [19], is required to deal with multiple orthogonal-plane current control. The complexity is expected to increase for higher phase-number machines.

(iii) Pre-defined discrete VVs, which are often of a point or line wise nature, limit the realizable voltage resolution, leading to unnecessarily higher but avoidable current ripples.

(iv) System non-idealities such as dead time, PWM delay, and measurement noises, are often ignored in the already complex predictive algorithm.

A logical solution to the above problems is through the CCS-MPC, explored rather rarely for multiphase drives (an exception is the work described in [20] and [21], which is related to a five-phase induction motor drive). An asymmetrical six-phase induction motor (ASIM), supplied by a two-level voltage source inverter, is considered here. The work commences with modeling of the ASIM while accurately accounting for the digital control and PWM delays. This work also hypothesizes that measurement noise, if not properly accounted for, would lead to negative impact on multiphase drives with very-high-bandwidth control and low sub-space reactance. To overcome this, a voltage-increment cost component is introduced, and its relevance is explained and proven. Dead-time effect is accounted for through a simple integrator-based reference augmentation. It is worth pointing out that PWM delay, measurement noise, and dead-time effect are rarely considered in most FCS-MPC designs, often because of partial VV space access. CCS-MPC attempts to nullify cost error on the control cycle basis, which means that accurate modelling and precise algorithm are relevant, if not critical. Also, the authors believe that this work is the first-ever application of the CCS-MPC to an asymmetrical six-phase drive, where the predictive control has been accurately designed considering the basic drive system's non-idealities. The closest to full CCS implementation is the one with hybrid CCS and FCS concepts [20], in which FCS still directly controls the switching states of the five-phase drives.

The rest of the paper is organized as follows: Section II introduces CCS-MPC's predictive model, associated modelling related to digital control and PWM delays, measurement noise, and dead-time effect, cost function, and post-optimization voltage limiting. Section III summarizes the classical proportional-integral-based field orientated control with current control in all planes. Section IV shows the experimental assessment. Section V concludes the paper.

II. CCS-MPC

CCS-MPC admits continuous control input set into the control algorithm. Generally, the two common ways to solve for the optimal control solution are: (i) analytical expression (unconstrained); (ii) quadratic programming (QP). In most cases of embedded control of power electronic converters the former is used because the latter in several-to-tens kHz embedded control is still prohibitive in practice [22]. It may become feasible in future as commercial embedded micro-controllers develop further. The CCS-MPC scheme is depicted graphically in Fig. 1.

A. Predictive Model

The ASIM's continuous-time state-space model, expressed in the synchronous reference frame, is:

$$\dot{\mathbf{x}}_c(t) = \mathbf{A}_c(t)\mathbf{x}_c(t) + \mathbf{B}_c\mathbf{u}_c(t)$$
$$\mathbf{y}_c(t) = \mathbf{C}_c\mathbf{x}_c(t) \tag{1}$$

where $\mathbf{x}_c$ is the state vector, $\mathbf{u}_c$ is the input vector, $\mathbf{y}$ is the output vector, expressible by

$$\mathbf{x}_c = \begin{bmatrix} i_{sd} & i_{sq} & i_{sx} & i_{sy} & \psi_{rd} & \psi_{rq} \end{bmatrix}^T$$
$$\mathbf{y}_c = \begin{bmatrix} i_{sd} & i_{sq} & i_{sx} & i_{sy} \end{bmatrix}^T \tag{2}$$
$$\mathbf{u}_c = \begin{bmatrix} v_{sd} & v_{sq} & v_{sx} & v_{sy} \end{bmatrix}^T$$

The corresponding time-variant state coefficient matrix $\mathbf{A}_c$, time-invariant input-coefficient matrix $\mathbf{B}$ and output-coefficient matrix $\mathbf{C}$ are given with the following expressions (standard definition of variables applies [4]), where $\omega^*_{se,t} = \omega_{re,t} + \omega^*_{sl,t}$, with $\omega^*_{sl} = i^*_{sq}/(T_r i^*_{sd})$):

$$\mathbf{A}_c(t) =$$

$$\begin{bmatrix}
-\left(\dfrac{1}{\sigma T_s} + \dfrac{1-\sigma}{\sigma T_r}\right) & \omega^*_{se,t} & 0 & 0 & \dfrac{1-\sigma}{\sigma L_m T_r} & \dfrac{(1-\sigma)\omega_{re,t}}{\sigma L_m} \\[2ex]
-\omega^*_{se,t} & -\left(\dfrac{1}{\sigma T_s} + \dfrac{1-\sigma}{\sigma T_r}\right) & 0 & 0 & -\dfrac{(1-\sigma)\omega_{re,t}}{\sigma L_m} & \dfrac{1-\sigma}{\sigma L_m T_r} \\[2ex]
0 & 0 & -\dfrac{R_s}{L_{ls}} & 0 & 0 & 0 \\[2ex]
0 & 0 & 0 & -\dfrac{R_s}{L_{ls}} & 0 & 0 \\[2ex]
\dfrac{L_m}{T_r} & 0 & 0 & 0 & -\dfrac{1}{T_r} & 0 \\[2ex]
0 & \dfrac{L_m}{T_r} & 0 & 0 & 0 & -\dfrac{1}{T_r}
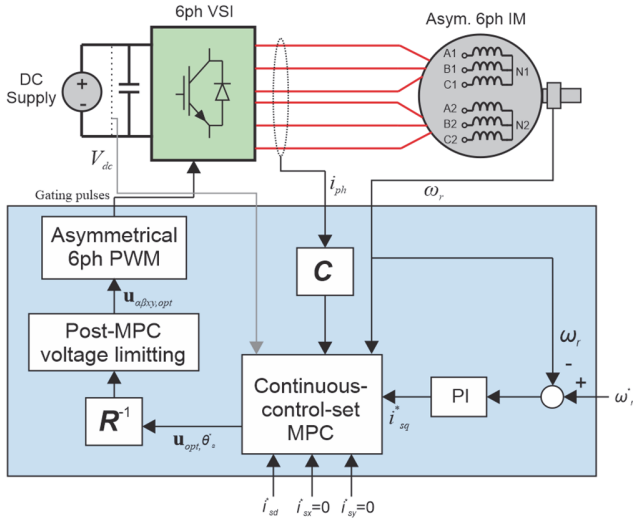\end{bmatrix}$$

Fig. 1: Continuous-control-set model predictive control of an asymmetrical six-phase induction motor drive.

$$\mathbf{B}_c = \begin{bmatrix} \dfrac{1}{\sigma L_s} & 0 & 0 & 0 \\ 0 & \dfrac{1}{\sigma L_s} & 0 & 0 \\ 0 & 0 & \dfrac{1}{L_{ls}} & 0 \\ 0 & 0 & 0 & \dfrac{1}{L_{ls}} \\ 0 & 0 & 0 & 0 \\ 0 & 0 & 0 & 0 \end{bmatrix} \quad \mathbf{C}_c = \begin{bmatrix} 1 & 0 & 0 & 0 & 0 & 0 \\ 0 & 1 & 0 & 0 & 0 & 0 \\ 0 & 0 & 1 & 0 & 0 & 0 \\ 0 & 0 & 0 & 1 & 0 & 0 \end{bmatrix} \quad (3)$$

The discrete state-space model with forward-Euler discretization (i. e. $\mathbf{A}_k = \mathbf{I} + \mathbf{A_c}T$) is:

$$\mathbf{x}_{k+1|k} = \mathbf{A}_k \mathbf{x}_k + \mathbf{B}\mathbf{u}_k \tag{4}$$
$$\mathbf{y}_k = \mathbf{C}\mathbf{x}_k$$

where $\mathbf{B} = \mathbf{B}_c T$ and $\mathbf{C} = \mathbf{C}_c$. It is worth noting that if flux-torque control is considered, higher-order discretization may be required to ensure accurate true-value tracking [23]. The observed quantity chosen here is the rotor flux, but other options such as rotor current [5] and stator/air-gap flux, are possible. With rotor-flux oriented control, this choice can lead to state-space order/size reduction, from 6th to 5th, following the zeroing of the q-axis rotor flux. The input vector is comprised of the primary plane (rotating-axis) and the secondary plane (stationary-axis) voltage vectors:

$$\mathbf{u}_k = \begin{bmatrix} e^{j\omega_{se,t}^* t} & \mathbf{0} \\ \mathbf{0} & e^0 \end{bmatrix} \mathbf{u}_{\alpha\beta xy} \tag{5}$$

where

$$\mathbf{u}_{\alpha\beta xy} = \begin{bmatrix} \mathbf{u}_{\alpha\beta} \\ \mathbf{u}_{xy} \end{bmatrix} = \frac{V_{dc}}{3} \mathbf{C} \begin{bmatrix} v_{a1} & v_{b1} & v_{c1} & v_{a2} & v_{b2} & v_{c2} \end{bmatrix}^T$$

$$\mathbf{C} = \frac{1}{3}\begin{bmatrix} e^{j0} & e^{j2\pi/3} & e^{j4\pi/3} & e^{j\pi/6} & e^{j5\pi/6} & e^{j\pi/2} \\ e^{j0} & e^{j2k_1\pi/3} & e^{j4k_1\pi/3} & e^{jk_1\pi/6} & e^{j5k_1\pi/6} & e^{jk_1\pi/2} \end{bmatrix}$$

$$(6)$$

It is well established that k_1 can be set to 5 to obtain the orthogonal secondary plane in ASIM model [24]. k_1 equal to 3

is for the zero-sequence plane, but it is irrelevant for current control with isolated neutrals.

It is important to accurately account for the system non-idealities in the model-based, high-bandwidth predictive control. In all existing FCS-MPC schemes, it is mandatory to account for the one cycle digital control implementation delay, which is often known as two-step/one-step-ahead mechanism [4], whereas the same delay is often disregarded in PI-based field-oriented control. For CCS-MPC in this work, a systematic approach is adopted from the outset. Typical non-idealities known in any practical drives system, e.g., digital control delay, PWM delay, measurement noise, and dead-time effect, will be considered.

B. Digital Implementation Delay

To account for the digital control delay, an additional step is added, resulting in the two-step predictive model:

First step: $\qquad \mathbf{x}_{k+1|k} = \mathbf{A}_k \mathbf{x}_k + \mathbf{B}\mathbf{u}_k \tag{7}$

Second step: $\dfrac{\mathbf{x}_{k+2|k} = \mathbf{A}_k \mathbf{x}_{k+1|k} + \mathbf{B}\mathbf{u}_{k+1|k}}{\mathbf{y}_{k+2|k} = \mathbf{C}\mathbf{x}_{k+2|k}} \tag{8}$

$\mathbf{u}_k$ is the optimal VV obtained from the previous $(k\text{-}1)^{\text{th}}$ control sampling instant, and $\mathbf{u}_{k+1|k}$ is the optimal VV to be computed from the present control cycle. It is necessary to assume that the machine speed is unchanged across the time steps so that the time-invariant model can simplify the solution. Note that this simplification is on per control cycle basis. In terms of closed-loop control, the controller still deals with time-variant plant (1), through MPC's open-loop optimization-based control.

C. PWM Delay

According to the modulation theory, for synchronous single-sampling system at the beginning of each modulation period, pulse width modulation has inherently a half-sample period delay [25]. This PWM delay is critical to be accounted for in phase-critical power electronic systems [26]. It has been considered in classical control of grid inverters with actively damped high-order filters [25] (typically through frequency response analysis). In the context of MPC, FCS-MPC only needs to account for the digital control delay. CCS-MPC, however, should in principle consider and compensate both digital control and PWM delays. To the best knowledge of the authors, the issue has not been addressed in any CCS-MPC work in power electronics. In the case of multiphase drives, owing to the unique characteristic of low secondary sub-space reactance, it becomes even more critical to account for PWM delay. This work therefore proposes a modification to (7)-(8) [4] to accurately account for the $1.5T_s$ delay. This consideration will be experimentally assessed and analyzed in Section IV-E. The changes are summarized as:

First step: $\qquad \mathbf{x}_{k+1|k} = \mathbf{A}_k \mathbf{x}_k + \dfrac{1}{2}\mathbf{B}\left(\mathbf{u}_k + \mathbf{u}_{k-1}\right) \tag{9}$

Second step: $\mathbf{x}_{k+2|k} = \mathbf{A}_k \mathbf{x}_{k+1|k} + \dfrac{1}{2}\mathbf{B}\left(\mathbf{u}_{k+1|k} + \mathbf{u}_k\right) \tag{10}$

$$\mathbf{y}_{k+2|k} = \mathbf{C}\mathbf{x}_{k+2|k}$$

Note that the sampling instant is an important factor for a correct delay compensation. The one above is designed for single synchronous sampling at the start of each modulation cycle.

D. Measurement Noise

Measurement noise is another important non-ideal feature to be accounted for in the motor drives control because of small time constants of electromagnetic circuits, especially in the auxiliary sub-spaces of multiphase machines. It is hypothesized that any current measurement noise, if not accounted for in the predictive control design, would logically be reflected directly in the "optimal" control action, i.e., optimal voltage, which may lead to slight performance deterioration. In highly inductive circuitry, the level of deterioration depends on the machine power, voltage, and speed rating.

In most reported FCS-MPC schemes with partial VV space access, the "most optimal" voltage vector is, from the full multi-dimensional VV space's point of view, slightly sub-optimal. Tracking errors resulting from such design (from full voltage space's point of view) may be indistinguishable from those induced by measurement noise. CCS-MPC, on the other hand, always attempts to nullify the tracking error in each control cycle. Therefore, its behavior with regard to the measurement noise is worth examining. In principle, this consideration and the conclusion drawn from it are extendable to advanced FCS-MPC schemes with cost error zeroing mechanism.

The impact of measurement noise is accounted for through the penalization of cost component formed by input voltage increments. The basis is that the controller can be made less "responsive" - tunable through an additional weighing factor – to the effects caused by the measurement noises. Hence, the predictive model is modified to the following form:

$$
\begin{aligned}
\mathbf{x}_{k+2|k} &= \mathbf{A}_k\left[\mathbf{A}_k\mathbf{x}_k + \frac{1}{2}\mathbf{B}\left(\mathbf{u}_k + \mathbf{u}_{k-1}\right)\right] + \frac{1}{2}\mathbf{B}\left(\mathbf{u}_{k+1|k} + \mathbf{u}_k\right) \\
&= \mathbf{A}_k^2\mathbf{x}_k + \frac{1}{2}\mathbf{A}_k\mathbf{B}\mathbf{u}_{k-1} + \left(\frac{1}{2}\mathbf{A}_k + \mathbf{I}\right)\mathbf{B}\mathbf{u}_k + \frac{1}{2}\mathbf{B}\Delta\mathbf{u}_{k+1|k}
\end{aligned} \tag{11}
$$

$$
\mathbf{y}_{k+2|k} = \mathbf{CA}_k^2\mathbf{x}_k + \frac{1}{2}\mathbf{CA}_k\mathbf{B}\mathbf{u}_{k-1} + \mathbf{C}\left(\frac{1}{2}\mathbf{A}_k + \mathbf{I}\right)\mathbf{B}\mathbf{u}_k + \frac{1}{2}\mathbf{CB}\Delta\mathbf{u}_{k+1|k}
$$

The effect of measurement noise, and the improvement due to the proposed modification, will be demonstrated experimentally in Section IV.

E. Cost Function and Optimal Solution

The full current tracking control with incremental input-voltage penalization is realized through the typical cost function of [27], [28]:

$$
J = \left(\mathbf{y}_{k+2}^* - \mathbf{y}_{k+2|k}\right)^T\mathbf{W}\left(\mathbf{y}_{k+2}^* - \mathbf{y}_{k+2|k}\right) + \Delta\mathbf{u}_{k+1|k}^T\mathbf{R}\Delta\mathbf{u}_{k+1|k} \tag{12}
$$

In principle, if online quadratic programming is computationally tractable under several-to-tens of kHz execution frequency, one can further append linear constraints, such as voltage and current limits, to the cost function and solve

for the optimal solution online. Nevertheless, considering the state-of-the-art microcontrollers, analytic solution that does not consider constraints is adopted here. The optimal incremental voltage input can be solved analytically:

$$
\frac{dJ}{d\Delta\mathbf{u}_{k+1|k}} = 0 \tag{13}
$$

Cost function (12) is re-formulated as (14), and the optimal input voltage increment is solved to give:

$$
\Delta\mathbf{u}_{k+1|k,opt} = \left(2\mathbf{R} + \frac{1}{2}\mathbf{B}^T\mathbf{C}^T\mathbf{WCB}\right)^{-1}\mathbf{B}^T\mathbf{C}^T\mathbf{W}\left(\mathbf{y}_{k+2}^* - \mathbf{CA}_k^2\mathbf{x}_k - \boldsymbol{\delta}_k\right) \tag{15}
$$

where $\boldsymbol{\delta}_k = \frac{1}{2}\mathbf{CA}_k\mathbf{B}\mathbf{u}_{k-1} + \mathbf{C}\left(\frac{1}{2}\mathbf{A}_k + \mathbf{I}\right)\mathbf{B}\mathbf{u}_k$.

It is worth noting that the penalization of incremental control action $\mathbf{R}$ will have direct implication for the inner control bandwidth. In principle, if $\mathbf{R}$ is kept low (as in Section IV-A), the inner loop's bandwidth will have a very wide/high bandwidth, which indirectly means that the outer speed loop can be easily decoupled, simplifying the overall tuning effort.

F. Post-optimization Voltage Limiting

The optimal VV to be imposed in the beginning of the next control cycle is computed using the optimal solution in (12) – (15):

$$
\mathbf{u}_{k+1|k,opt} = \mathbf{u}_k + \Delta\mathbf{u}_{k+1|k,opt} \tag{16}
$$

During large transients and operation near overmodulation region, this VV may exceed the physical limit of the voltage space vector. For linear modulation, the magnitude sum of the orthogonal single-/two-dimensional voltage vectors should be confined to less than the physically realizable maximum magnitude. For simplicity, overmodulation is not considered here, and a simple dc bus voltage pre-allocation is adopted. Interested readers are referred to [29] and references therein for other considerations on overmodulation in CCS-MPC. In [29], solutions of overmodulation/constrained mode are investigated together with the theoretical analysis of noise in Linear Quadratic Regulator (i.e., an unconstrained MPC with an infinite horizon).

The maximum realizable magnitudes of the voltage vectors in the primary and secondary planes are fixed at, respectively, 94% and 6% (note: this selection is informed by the magnitude of xy-voltages deployed by the classical PI-based control). In both planes, when the magnitude exceeds the predefined limit, the voltage vector will be truncated (i.e., scaled down to the circular border). This consideration is illustrated graphically in Fig. 2. Another property worth emphasizing here is the feature of full vector space access. In the proposed CCS-MPC, the entire, yellow-shaded region can be accessed by CCS-MPC without any restriction on its location in the voltage vector spaces in Fig. 2 (e.g., in the context of PWM-integrated FCS-

$$
\begin{aligned}
J &= \left(\mathbf{y}_{k+2}^* - \mathbf{CA}_k^2\mathbf{x}_k - \boldsymbol{\delta}_k - \frac{1}{2}\mathbf{CB}\Delta\mathbf{u}_{k+1|k}\right)^T\mathbf{W}\left(\mathbf{y}_{k+2}^* - \mathbf{CA}_k^2\mathbf{x}_k - \boldsymbol{\delta}_k - \frac{1}{2}\mathbf{CB}\Delta\mathbf{u}_{k+1|k}\right) + \Delta\mathbf{u}_{k+1|k}^T\mathbf{R}\Delta\mathbf{u}_{k+1|k} \\
&= \left[\left(\mathbf{y}_{k+2}^* - \mathbf{CA}_k^2\mathbf{x}_k - \boldsymbol{\delta}_k\right)^T - \frac{1}{2}\Delta\mathbf{u}_{k+1}^T\mathbf{B}^T\mathbf{C}^T\right]\mathbf{W}\left[\left(\mathbf{y}_{k+2}^* - \mathbf{CA}_k^2\mathbf{x}_k - \boldsymbol{\delta}_k\right) - \frac{1}{2}\mathbf{CB}\Delta\mathbf{u}_{k+1|k}\right] + \Delta\mathbf{u}_{k+1|k}^T\mathbf{R}\Delta\mathbf{u}_{k+1|k} \\
&= \left[\left(\mathbf{y}_{k+2}^* - \mathbf{CA}_k^2\mathbf{x}_k - \boldsymbol{\delta}_k\right)^T\mathbf{W}\left(\mathbf{y}_{k+2}^* - \mathbf{CA}_k^2\mathbf{x}_k - \boldsymbol{\delta}_k\right) - \Delta\mathbf{u}_{k+1}^T\mathbf{B}^T\mathbf{C}^T\mathbf{W}\left(\mathbf{y}_{k+2}^* - \mathbf{CA}_k^2\mathbf{x}_k - \boldsymbol{\delta}_k\right)\right] + \\
&\quad \Delta\mathbf{u}_{k+1|k}^T\left(\mathbf{R} + \frac{1}{4}\mathbf{B}^T\mathbf{C}^T\mathbf{WCB}\right)\Delta\mathbf{u}_{k+1|k}
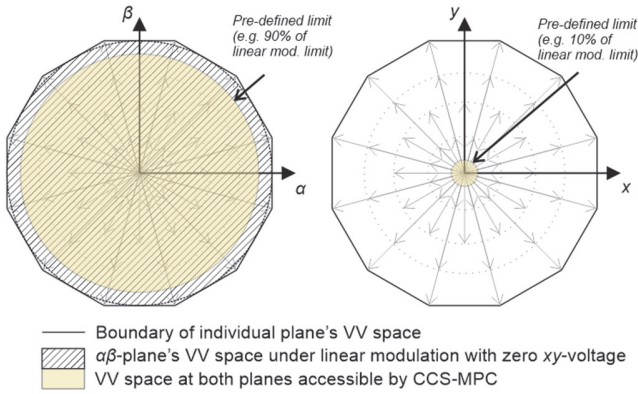\end{aligned} \tag{14}
$$

Fig. 2: Primary and secondary plane's voltage vector spaces highlighting the regions accessible by CCS-MPC.
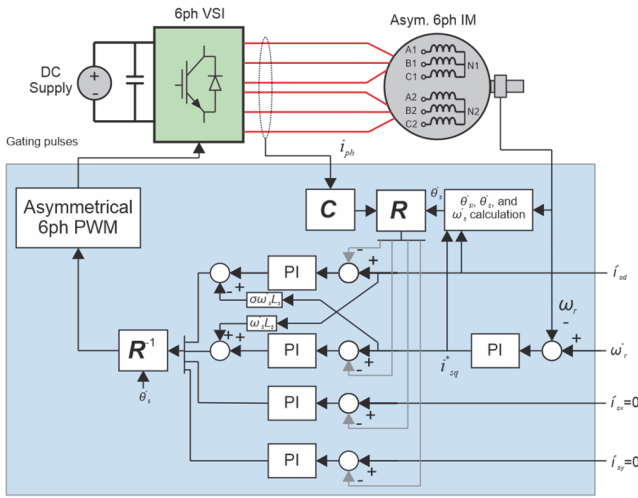

Fig. 3: Classical PI-based field-oriented control of an asymmetrical six-phase induction motor drive.

TABLE I.   PARAMETERS OF ASYMMETRICAL SIX-PHASE INDUCTION MOTOR DRIVE SYSTEM

Symbol	Parameters	Values
F_s	IM rated frequency	50 Hz
p	IM pole numbers	2
R_s, R_r	IM stator, rotor phase resistances	12 Ω, 4 Ω
L_{ls}, L_{lr}	IM stator, rotor leakage inductance	60 mH, 60 mH
L_m	IM mutual inductance	880 mH
σ	IM leakage factor	0.124
V_{dc}	VSI dc-bus voltage	300 V
F_s	Control sampling frequency	8 kHz
V_{base}, I_{base}	Base voltage, base current	173 V, 10 A
-	Dead time	6 μs

MPC schemes, the so-called "restriction" means finite-number of "dots" or "lines" in the spaces [6]-[11], [16], [17]).

G. Dead-time Effect and Compensation

As shown in [30], [31] for grid current control, dead-time effect is evidently very relevant in MPC schemes with cycle-by-cycle cost error zeroing. This phenomenon is explained as follows: dead-time effect is fundamentally non-linear and state-dependent. Since the linear predictive model assumes that the inverter behaves as an ideal amplifier, there always exist prediction errors regardless of the type of the cost function, absolute or incremental. Note that dead-time effect is usually
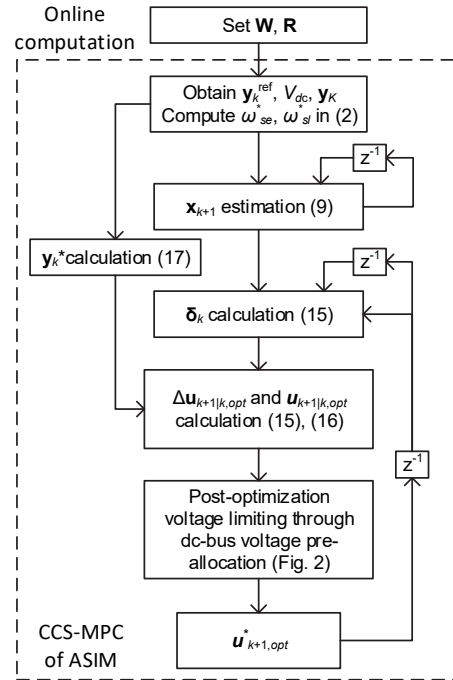

Fig. 4: CCS-MPC algorithm for the asymmetrical six-phase drive. Note that online computation of matrices in (15)-(16) is kept at minimum to enable real-time execution of the algorithm at 8 kHz control sampling frequency.

harder to detect in FCS-MPC with broad switching spectrum, e.g. five-phase drives [4]. One possible solution is through modifying the predictive model to account for the inherent voltage error in the open-loop manner [30], [31]. Alternatively, a simpler closed-loop means where the references are augmented with integrators prior to the optimization stage, can be adopted. Both methods primarily target the fundamental component of tracking errors caused by dead-time voltage errors with triplen harmonics. The latter is adopted here:

$$\mathbf{y}_k^* = \mathbf{y}_k^{ref} + \Delta\mathbf{y}_k^{int}$$
$$\Delta\mathbf{y}_k^{int} = \Delta\mathbf{y}_{k-1}^{int} + k_{int}\left(\mathbf{y}_k^{ref} - \mathbf{y}_k\right) \quad (17)$$

where $\mathbf{y}^{ref}$ is the original reference supplied externally and $\mathbf{y}^*$ is the augmented reference fed into the predictive control algorithm. A careful consideration is necessary to decouple the tuning of integrator gain K_{int} from the main dynamic control loop. This is done through a small enough K_{int} value, i.e., one that gives time constant of several seconds duration.

III. CLASSICAL FIELD-ORIENTED CONTROL

A. Full Current Control Based on PI-FOC

Classical, PI-based full current control of ASIM with two isolated neutrals is effectively the same as that used in a five-phase induction motor. Fig. 3 shows the corresponding control schematic implemented in this work. In the interest of space, interested readers may refer to [4] (and references therein) for design details. The main differences are the inverter model, decoupling transformation, and pulse width modulator. The proportional and integral gains of all four PI controllers are tuned empirically in the experiments.
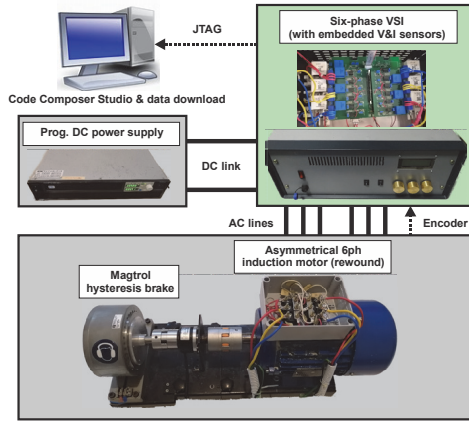
Fig. 5: Laboratory test rig of the asymmetrical six-phase induction motor drive used for the control scheme assessment.
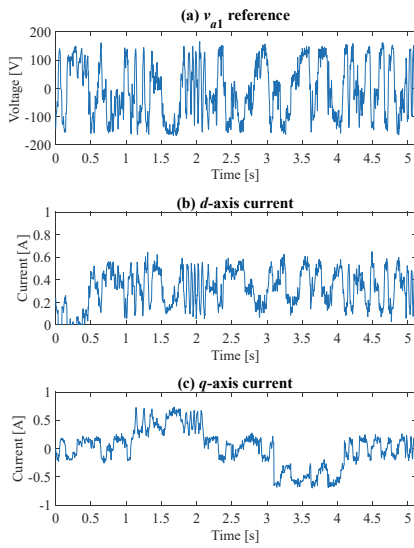

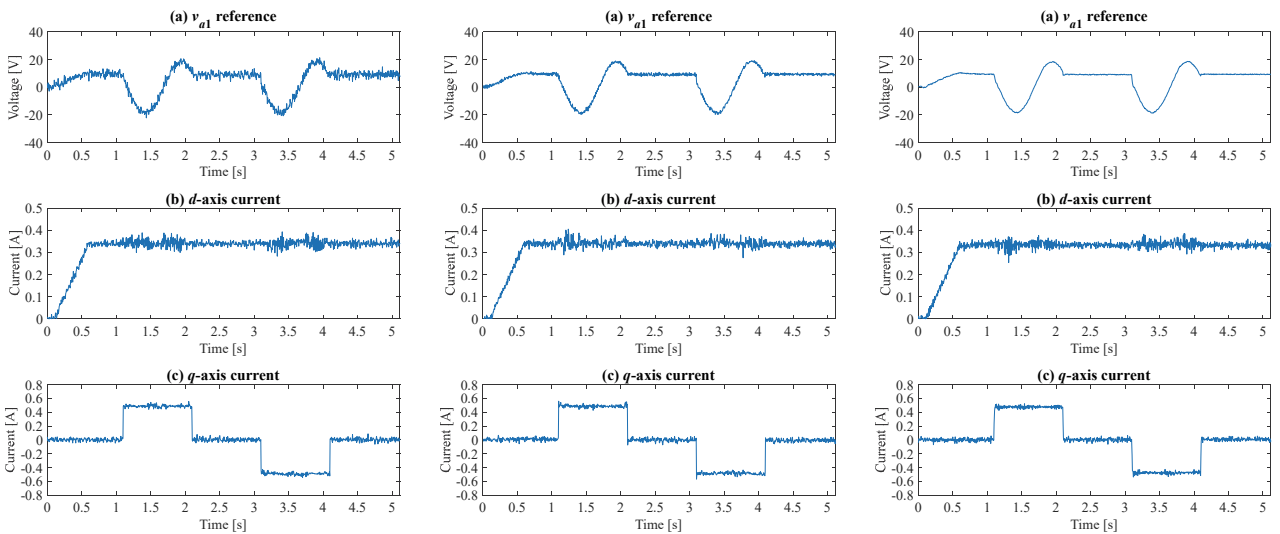Fig. 6: Failure of the predictive control to regulate the machine currents at R = 0.00001*I.

B. Asymmetrical Six-phase Pulse Width Modulation

There are several asymmetrical six-phase PWM schemes [32]. This work adopts carrier-based pulse width modulation with min-max injection (per three-phase circuits), which is essentially equivalent to two three-phase inverters based SVPWM [33]. CCS-MPC uses the same PWM scheme.

IV. EXPERIMENTAL RESULTS

Flowchart of the CCS-MPC algorithm described in Section III is shown in Fig. 4. The developed predictive control scheme is examined experimentally in the laboratory test rig shown in Fig. 5. It consists of 2-pole (10/12 pitch) asymmetrical six-phase induction motor rewound from a 1.5 hp three-phase induction motor (415 V, 50 Hz, 4-pole, 24-slot), a custom-made six-phase voltage source inverter constructed using Semikron's IGBT SKM50GB12V, iDRC's dc voltage supply, and Magtrol's hysteresis brake. The test rig is depicted graphically in Fig. 5. The six-leg inverter is controlled by Texas Instrument DSP microcontroller TMS320F28335. Each inverter leg's output current is measured using LEM LA25P and the measurement signal is conditioned with very minimum analog filtering to preserve phase integrity. Dc-bus voltage is reduced to 300V to allow a safe testing and live online weighting factor tuning. The machine parameters used in the predictive model are obtained experimentally through standard no-load and locked-rotor tests, using the hysteresis brake. The machine-inverter parameters and other experimental system settings are given in Table I.

A. Measurement Noise Compensation

The relevance of the incremental input voltage weighting is assessed first. The machine's d-axis current reference is ramped from 0 A to 0.35 A to realize gradual flux build-up during initialization. The q-axis current reference is stepped through the values of 0, 0.5, -0.5, and 0 A, with each step lasting one second. Note that throughout this part of the investigation, the rotor is intentionally locked using the hysteresis brake in order to remove any discrepancy that could be caused by rotor vibration across different gain values. First, weighting factor W is set to I and weighting factor R is set to near zero value, i.e.,

Fig. 7: Measurement noise effect and its compensation. (Left col.) R = 0.0001*I; (Middle col.) R = 0.001*I; (Right col.) R = 0.01*I.

to 0.00001*$\mathbf{I}$, where $\mathbf{I}$ is an identity matrix of an appropriate dimension. In principle, the predictive control should continue to function through the current tracking part of the cost function (12). However, Fig. 6 shows that the predictive controller failed to satisfactorily regulate the machine currents. This is deduced to be caused by the measurement noise. Next, weighting factor $\mathbf{R}$ is set to 0.0001, 0.001, and 0.01 ($\mathbf{I}$ is omitted from notation herein), and the corresponding current waveforms are shown in Fig. 7. It is seen that, as $\mathbf{R}$'s magnitude increases, the waveform of the optimal voltage (only phase-A voltage reference is shown, computed on-the-fly using multi-leg inverter's duty ratios) contains increasingly less white-noise-like ripples (in this low-power test rig, effect on currents is not significant). This result evidently supports the hypothesis about the effect of measurement noise in CCS-MPC. The input voltage penalization is therefore relevant, and functions as intended. Another remark on $\mathbf{R}$ is that if its value is set to a much higher value, e.g, few tens of times above the range considered here, the current dynamics will be noticeably slower. $\mathbf{R}$ is set to 0.005 for subsequent tests.

The above phenomenon is explained further in conjunction with all the control schemes considered in this work. In the classical, PI-based FOC, the explanation is straightforward. The low-bandwidth PI controllers have negligible gains in the vicinity of the frequency spectrum of the measurement, making it irrelevant during controller design. In FCS-MPC, the finite number of switching states or voltage vectors, actual or virtual, means that the cost function error is normally not nullified in each control cycle (at steady state). Therefore, the measurement noise contributes to enlarging the cost function error, affecting, though minimally (in close proximity from the theoretically optimal solution), the search for the optimal discrete VVs. If the "natural" voltage ripple is larger than what would be caused by the measurement noise (like in Fig. 7), the impact is less obvious. On the contrary, CCS-MPC has full VV space access with cost error zeroing feature. Significant measurement noise, when left uncompensated, causes seemingly unregulated currents, as shown in Fig. 5. Despite that, it is worth highlighting that the closed-loop system has not become unstable.

B. Dead-time Effect Compensation

Quality of the primary plane's d-axis current tracking is assessed against the dead-time effect and the proposed simple, integrator-based compensation. Fig. 8 shows d-axis current waveforms for uncompensated and compensated scenarios, with the d-axis current reference ramped to 0.35 A and then kept constant. Zoomed-view of the uncompensated d-axis current confirms the existence of steady-state tracking error, which is expected to be present also in the q-axis current (not shown). The extent of steady-state error depends on dead time, switching frequency, machine rating, and dc-bus voltage magnitude. Steady-state current tracking errors are relevant for the accurate control of the machine's flux level, and of the motor torque for drive systems operating in the torque control mode. With integral gain k_{int} set as 0.01 (i.e., an empirical value obtained through a simple live tuning), the steady-state tracking error is eliminated. This provides a simple proof of the effectiveness of the proposed compensation. It is worth noting
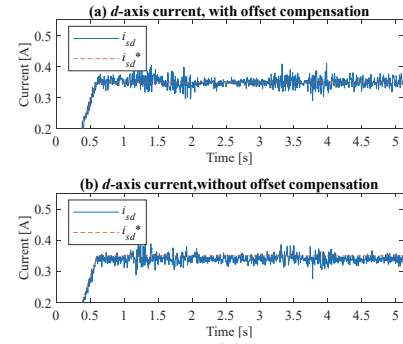

Fig. 8: Stator d-axis current tracking (a) with dead-time compensation; (b) without dead-time compensation.
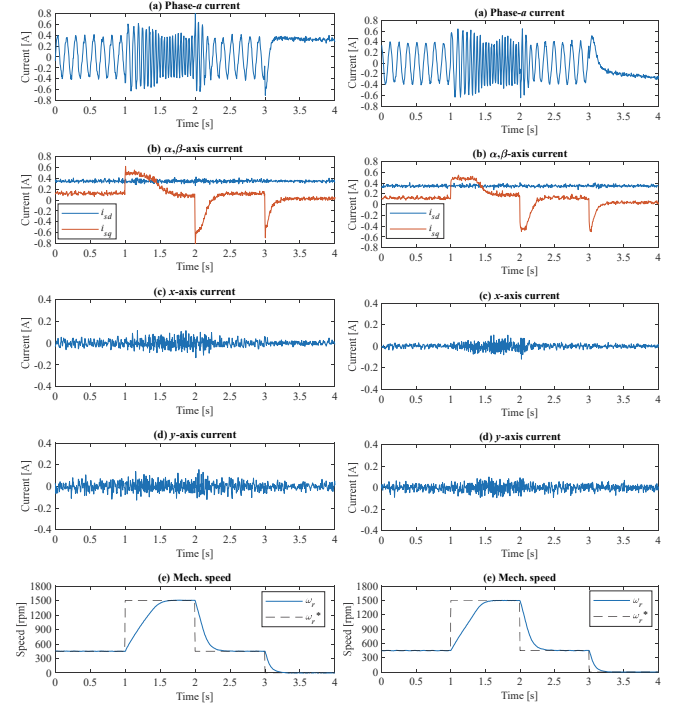

Fig. 9: Current waveforms during the torque transient and reversal in (left col.) CCS-MPC and (right col.) PI-based field-oriented control. Reference speed is stepped from 450 rpm to 1500 rpm and the back to 0 rpm at 1, 2, and 3 s, respectively. Reference i^*_{sd} is kept constant at 0.35 A. DSP data sampling freq. is set as 200 Hz.

that the tuning of the integrator gain k_{int} is significantly simpler, when compared to the integral gains in the main PI controller of the classical control scheme, where closed-loop dynamic performance matters.

C. Torque Transient and Reversal – Comparative Assessment

Next, the torque transient and reversal in both CCS-MPC and the classical PI-based field-oriented control are examined, and the selected waveforms are shown in Fig. 9. The same PI-based speed control loop is inserted as the outer loop of both current control schemes. PI controllers in all four current control loops, especially those in the primary plane, have been tuned empirically to result in sufficiently fast current transients. On the contrary, apart from the tuning of $\mathbf{R}$, required for input voltage penalization, CCS-MPC requires minimum tuning.

On examining Fig. 9 further, small differences in current and speed transients can be noticed. CCS-MPC exhibits slightly
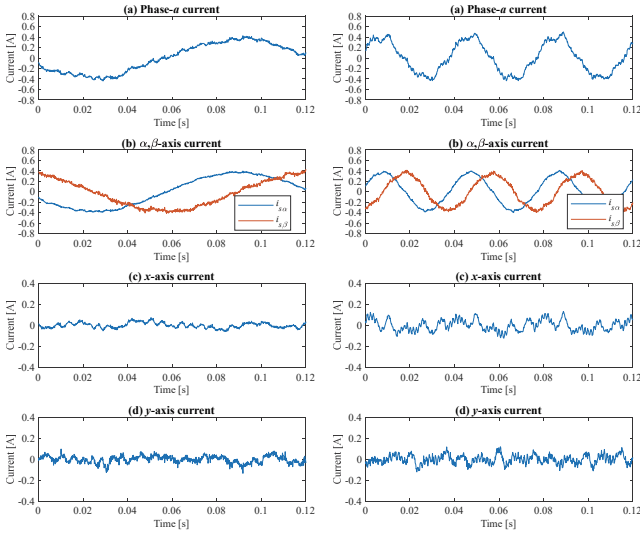
Fig. 10: CCS-MPC with PWM. (Left col.) 0.15 pu speed ref; (Right col.) 0.5 pu speed ref. DSP data sampling freq. is set as 4 kHz.
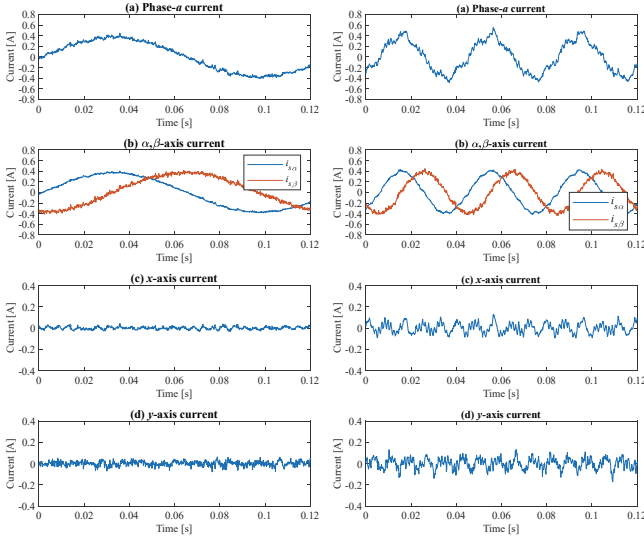

Fig. 11: PI-based full current control with PWM. (Left col.) 0.15 pu speed ref; (Right col.) 0.5 pu speed ref. DSP data sampling freq. is 4 kHz.

faster transients with small overshoots in q-axis currents (evidenced in the speed waveform too) during large step change of the current references. The overshoots are deduced to be caused by slight parameter mismatch. On the other hand, the classical control scheme exhibits a good transient response due to a rather lengthy (live) tuning of the PI gains. In terms of steady-state x-, y-axis current ripples, given the control and gain settings, CCS-MPC is characterized with somewhat higher ripples, which is explained by imperfect matching of parameters in the control algorithm and the real system. It is worth pointing out that the above is in fact a result of careful tuning of the proportional gain of the PI controllers. A larger proportional gain will give higher sub-space current ripples than what is shown in Fig. 9 (right column), due to direct measurement noise amplification effect.

D. Steady-state Performance – Comparative Assessment

The steady-state performance for the used parameter/gain settings is examined further in Figs. 10 and 11. Fig. 10 shows the phase-$a1$, σ-, β-, x-, and y-axis currents of the asymmetrical six-phase machine at 450 and 1500 rpm for the CCS-MPC scheme. Fig. 11 shows the exact counterpart for the PI-based field-oriented control scheme. The reduced maximum speed range (1500 rpm) is a direct consequence of using one half of the rated dc-bus voltage at (near) rated flux/d-axis current – a value obtainable through scalar control. Two observations are made here:

(i) in terms of high-order harmonics, i.e., switching ripples near 8 kHz switching frequency (see both Figs. 10 and 11), despite slight aliasing due to down sampling, both control schemes are practically equivalent. Both control schemes possess higher switching ripples at high operating speed (1500 rpm) than that at low operating speeds because MMF harmonics are effectively higher due to lower number of switchings per fundamental cycle. The entire voltage vector space is deployable by both control schemes. Also, the design basis of CCS-MPC does not require explicit consideration of the individual orthogonal planes and discrete VVs, actual or virtual. Therefore, the proposed predictive control scheme can be easily generalized to motor drives of higher phase order, e.g., three-plane current control in seven-phase drives.

(ii) in terms of low-order harmonics, the x-, y-plane currents of CCS-MPC are still somewhat higher than in the case of classical control counterpart. It is noticed that the current distortion caused by dead-time effect, of harmonic orders higher than three, cannot be fully eliminated by the present design. This is because only the dc steady-state error can be eliminated (i.e., in classical control context, very high controller gain at dc). It is also noted that the low-order current distortion is slightly more pronounced for CCS-MPC at low operating speed as compared to that in the classical control scheme, deduced to be caused by parameter mismatch. At higher speeds, both control schemes exhibit quite similar behavior.

The operating current of CCS-MPC at 1500 rpm (logged using oscilloscope at 25 kHz sampling frequency) and its post-processed frequency spectrum is shown in Fig. 12. First, the main (high) frequency switching harmonics are concentrated around the 8 kHz region. Second, the presence of the 5th order harmonic, which maps into the xy-plane (according to the harmonic mapping principle [34]), confirms the discussion about limited correction gain of CCS-MPC on ac components.

E. Further Assessment of PWM Delay Compensation, Loading, and Parameter Mismatch

The effect of PWM delay and the relevance of the proposed model improvement are examined next using a second asymmetrical six-phase motor drive test rig, different from that described in Table I. Subsequent sets of results are obtained using this test rig. The rig's parameters, the experimental conditions, and settings, are described in the caption of Fig. 13. Fig. 13a shows the phase and sub-space currents produced by CCS-MPC with uncompensated PWM delay, i.e., through model (7)-(8). The counterpart of (15) is:

$$\Delta\mathbf{u}_{k+1|k,opt,uncomp} = \left(\mathbf{R} + \mathbf{B}^T\mathbf{C}^T\mathbf{WCB}\right)^{-1}\mathbf{B}^T\mathbf{C}^T\mathbf{W}\left(\mathbf{y}_{k+2}^* - \mathbf{CA}_k^2\mathbf{x}_k - \boldsymbol{\delta}_k\right)$$
(18)

where $\boldsymbol{\delta}_{k,uncomp} = \mathbf{C}\left(\mathbf{I} + \mathbf{A}_k\right)\mathbf{B}\mathbf{u}_k$.

Fig. 13b shows the counterpart of Fig. 10's left column for 450 rpm speed reference at no load, and with PWM delay compensated using models (9)-(10). It can be clearly seen that currents in the xy-plane are more susceptible to PWM delay because the auxiliary (secondary) planes have only leakage reactance in multiphase drives system. This evidently supports the discussion on the susceptibility of non-idealities on multiphase drives' predictive control. Moreover, it can be seen from Figs. 13a and 13b that the $\alpha\beta$-plane's currents deteriorate due to higher xy-current ripple, due to single cost function control mechanism. With PWM delay compensated, Fig. 14 shows the current waveforms under higher passive loading, imposed by a mechanically coupled permanent magnet synchronous machine connected to an adjustable power resistor.

The effect of parameter mismatch on steady-state current waveforms is examined next. Figs. 15-17 show the sub-plane currents for the mismatches of, respectively, stator leakage inductance, magnetizing inductance, and stator resistance. It is clearly evidenced that CCS-MPC requires an accurate leakage inductance to produce high-quality current waveforms, as the mismatch affects the regulation quality of the xy-plane currents. Similarly, with single cost function, $\alpha\beta$-plane currents are
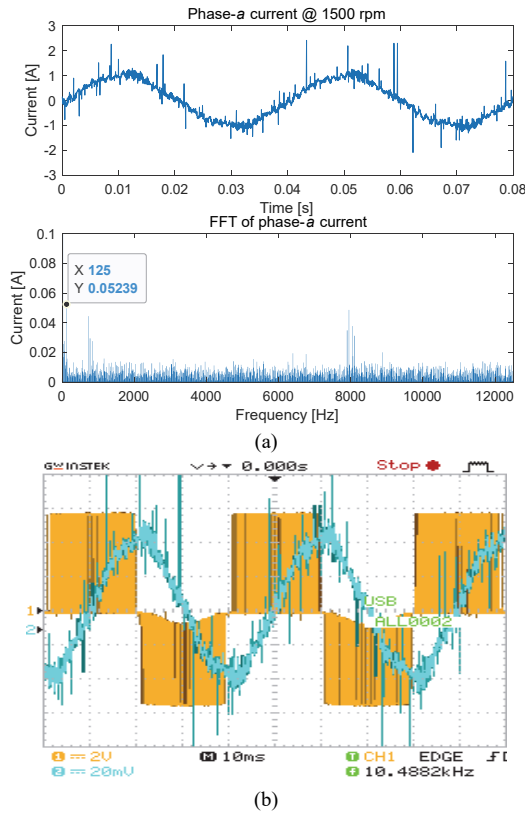

Fig. 12: (a) Phase current and its frequency spectrum of CCS-MPC operating at 1500 rpm. (b) Corresponding oscilloscope's screen shot (with default time window). Oscilloscope sampling frequency is 25 kHz. (Scaling: 2V/100V (Ch1), 20mV/500mA (Ch2)).
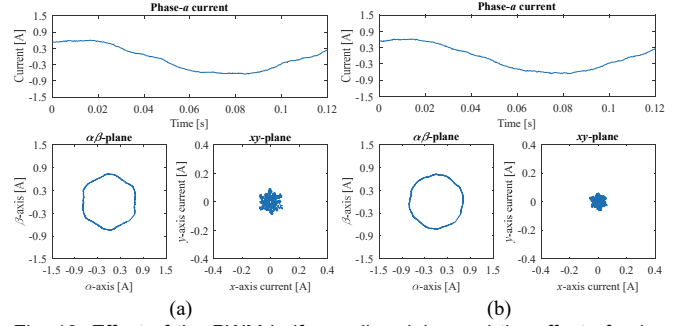

Fig. 13: Effect of the PWM half-sampling delay and the effect of using the improved predictive model in CCS-MPC, with the motor running at 450 rpm without loading. (a) Standard two-step predictive model (7)-(8); (b) improved predictive model (9)-(10). All other experimental conditions remain the same. A second asymmetrical six-phase motor drive, different from that described in Table I, is used. [Machine parameters: 1.5 kW, 24 slots, 2 poles, 10/12 pitch, R_{s1} = 8 Ω, R_{r1} = 4 Ω, L_{m1} = 572 mH, $L_{s1} = L_{r1}$ = 30 mH; Dc-bus voltage is 200V; switching frequency 8 kHz; dead time 4.5 μs; flux/d-axis current reference is 0.7 A].
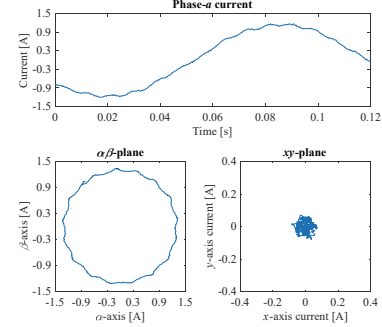

Fig. 14: Steady-state phase and sub-space currents when motor runs at 450 rpm with load.
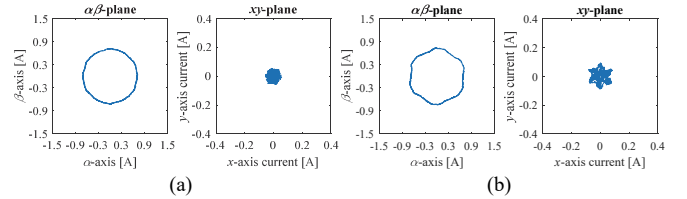

Fig. 15: Effect of stator leakage inductance mismatch (as compared to the nominal L_{ls1} used in Figs. 13-14) on sub-space currents. (a) 50% L_{ls1}; (b) 200% L_{ls1}.
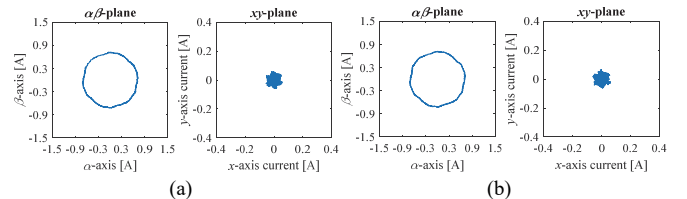

Fig. 16: Effect of magnetizing inductance mismatch (as compared to nominal L_{m1} used in Figs. 13-14) on sub-space currents. (a) 50% L_{m1}; (b) 200% L_{m1}.
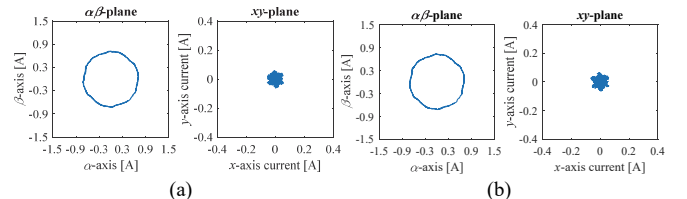

Fig. 17: Effect of stator resistance mismatch (as compared to R_{s1} used in Figs. 13-14) on sub-space currents. (a) 50% R_{s1}; (b) 200% R_{s1}.

TABLE II. SUMMARY OF COMPARATIVE ASSESSMENT

Performance	CCS-MPC	Classical FOC
Switching frequency	8 kHz	8 kHz
Current THD @ 450 rpm	11.2%	8.7 %
Current THD @ 1500 rpm	7.3 %	5.8 %
Current dynamics, and its tuning	Consistently fast. **R** dependent, very simple	Fast, with cross-decoupling and well tuned PI gains.
Cost function design	Less flexible, limited to linear cost function design	-
Ability to consider constraints dynamically	Not available in analytical optimal solution. Voltage is explicitly constrained.	Through anti-windup mechanism. Voltage is explicitly constrained.
Parameter sensitivity impact on dynamic and steady-state performances	Similar impact on dynamics. Current quality depends on L_{ls}, but is insensitive to L_m and R_s. Non-switching voltage ripple is **R** dependent.	Similar impact on dynamics. Current quality depends mainly on P gain, and is insensitive to L_{ls}, L_m and R_s.
Digital control and PWM delays	Susceptible, but can be compensated.	Not susceptible in most practical cases
Computational time*	Medium	Low

* For CCS-MPC, real-time matrix multiplication is minimized by pre-multiplying some matrices offline.

inevitably affected. Fig. 16 shows that the magnetizing inductance (and rotor resistance) mismatch has little impact on the steady-state current quality, but the machine transient is inevitably affected more. This is a well-established subject, and interested readers are referred to [4] and references therein for details. Fig. 17 shows that the impact of stator resistance mismatch is not as significant when compared to that of stator leakage reactance. Lastly, Table II summarizes the comparative numerical assessment values.

V. CONCLUSION

CCS-MPC of an asymmetrical six-phase induction motor drive is presented. The designed cost function deals with the tracking of the multiple plane's current components, and measurement noise suppression through penalization of input voltage increments. The design accurately considers the presence of non-idealities, namely digital control delay, PWM delay, and dead time. The proposed control scheme is assessed experimentally and compared with the classical PI-based field-oriented control. The comparison reveals that the CCS-MPC has similar switching performance as the PWM-based classical control. It is also concluded that the CCS-MPC performance is affected by the problems caused by the dead-time-induced low-order harmonics and parameter mismatch. These aspects should be investigated and improved further to increase the industrial relevance of the predictive control scheme for constant-switching frequency low-/medium-power multiphase drives.

Most recent FCS-MPC schemes for multiphase drives by and large face the design challenges posed by large number of actual/virtual VVs and multiple orthogonal planes in the context of full current control. In principle, if linear predictive model and time-invariant assumptions (within each control cycle) are adopted, the achievable steady-state performance of those FCS-MPC schemes is at best equivalent to CCS-MPC. The explicit consideration of multiphase voltage vectors in CCS-MPC effectively moves the switching voltage synthesis back to the established pulse width modulator. In the context of the algorithmic complexity resulting from dealing with

multiphase system's large number of active voltage vectors and meeting full current control requirement, the form of CCS-MPC discussed in the paper has some advantages over the present FCS's state of the art, especially in systems with higher phase order and/or in systems supplied from multilevel inverters. The work however concludes that CCS-MPC, despite the attempted accurate design considering non-idealities, does have the problems of low-order harmonics (due to parameter mismatch) and implicit constraints consideration. These can be the next direction of research.

REFERENCES

[1] F. Barrero and M. J. Duran, "Recent Advances in the Design, Modeling, and Control of Multiphase Machines—Part I," *IEEE Trans. Ind. Electron.*, vol. 63, no. 1, pp. 449–458, Jan. 2016, doi: 10.1109/TIE.2015.2447733.

[2] P. Gonçalves, S. Cruz, and A. Mendes, "Finite Control Set Model Predictive Control of Six-Phase Asymmetrical Machines—An Overview," *Energies*, vol. 12, no. 24, Art. no. 24, Jan. 2019, doi: 10.3390/en12244693.

[3] M. Bermúdez, C. Martín, I. González-Prieto, M. J. Durán, M. R. Arahal, and F. Barrero, "Predictive current control in electrical drives: an illustrated review with case examples using a five-phase induction motor drive with distributed windings," vol. 14, no. 8, pp. 1291–1310, Jun. 2020.

[4] C. S. Lim, E. Levi, M. Jones, N. Abd. Rahim, and W. P. Hew, "FCS-MPC-Based Current Control of a Five-Phase Induction Motor and its Comparison with PI-PWM Control," *IEEE Trans. Ind. Electron.*, vol. 61, no. 1, pp. 149–163, Jan. 2014, doi: 10.1109/TIE.2013.2248334.

[5] F. Barrero, M. R. Arahal, R. Gregor, S. Toral, and M. J. Duran, "A Proof of Concept Study of Predictive Current Control for VSI-Driven Asymmetrical Dual Three-Phase AC Machines," *IEEE Trans. Ind. Electron.*, vol. 56, no. 6, pp. 1937–1954, Jun. 2009, doi: 10.1109/TIE.2008.2011604.

[6] I. Gonzalez-Prieto, M. J. Duran, J. J. Aciego, C. Martin, and F. Barrero, "Model Predictive Control of Six-Phase Induction Motor Drives Using Virtual Voltage Vectors," *IEEE Trans. Ind. Electron.*, vol. 65, no. 1, pp. 27–37, Jan. 2018, doi: 10.1109/TIE.2017.2714126.

[7] M. Ayala, J. Doval-Gandoy, J. Rodas, O. Gonzalez, R. Gregor, and M. Rivera, "A Novel Modulated Model Predictive Control Applied to Six-Phase Induction Motor Drives," *IEEE Trans. Ind. Electron.*, vol. 68, no. 5, pp. 3672–3682, May 2021, doi: 10.1109/TIE.2020.2984425.

[8] O. Gonzalez, M. Ayala, J. Rodas, R. Gregor, G. Rivas, and J. Doval-Gandoy, "Variable-Speed Control of a Six-Phase Induction Machine using Predictive-Fixed Switching Frequency Current Control Techniques," in *2018 9th IEEE International Symposium on Power Electronics for Distributed Generation Systems (PEDG)*, Jun. 2018, pp. 1–6. doi: 10.1109/PEDG.2018.8447837.

[9] Y. Luo and C. Liu, "Elimination of Harmonic Currents Using a Reference Voltage Vector Based-Model Predictive Control for a Six-Phase PMSM Motor," *IEEE Trans. Power Electron.*, vol. 34, no. 7, pp. 6960–6972, Jul. 2019, doi: 10.1109/TPEL.2018.2874893.

[10] M. S. R. Saeed, W. Song, B. Yu, and X. Wu, "Low-Complexity Deadbeat Model Predictive Current Control With Duty Ratio for Five-Phase PMSM Drives," *IEEE Trans. Power Electron.*, vol. 35, no. 11, pp. 12085–12099, Nov. 2020, doi: 10.1109/TPEL.2020.2983048.

[11] T. Tao, W. Zhao, Y. He, J. Zhu, H. Tan, and R. Xue, "Multivector Predictive Current Control for Five-Phase PM Motor by Using Hybrid Duty Modulation Technology," *IEEE Trans. Transp. Electrification*, vol. 6, no. 4, pp. 1603–1612, Dec. 2020, doi: 10.1109/TTE.2020.2991080.

[12] W. Song, C. Xue, X. Wu, and B. Yu, "Modulated Finite-Control-Set Model Predictive Current Control for Five-Phase Voltage-Source Inverter," *IEEE Trans. Transp. Electrification*, vol. 7, no. 2, pp. 718–729, Jun. 2021, doi: 10.1109/TTE.2020.3019208.

[13] W. Zhao, H. Wang, T. Tao, and D. Xu, "Model Predictive Torque Control of Five-Phase PMSM by Using Double Virtual Voltage Vectors Based on Geometric Principle," *IEEE Trans. Transp. Electrification*, vol. 7, no. 4, pp. 2635–2644, Dec. 2021, doi: 10.1109/TTE.2021.3063193.

[14] M. H. Holakooie, G. Iwanski, and T. Miazga, "Switching-Table-Based Direct Torque Control of Six-Phase Drives with x y Current Regulation," *IEEE Trans. Ind. Electron.*, pp. 1–1, 2022, doi: 10.1109/TIE.2021.3139239.

[15] C. Xiong, H. Xu, T. Guan, and P. Zhou, "A Constant Switching Frequency Multiple-Vector-Based Model Predictive Current Control of Five-Phase PMSM With Nonsinusoidal Back EMF," *IEEE Trans. Ind. Electron.*, vol. 67, no. 3, pp. 1695–1707, Mar. 2020, doi: 10.1109/TIE.2019.2907502.

[16] Y. Luo and C. Liu, "Model Predictive Control for a Six-Phase PMSM Motor With a Reduced-Dimension Cost Function," *IEEE Trans. Ind. Electron.*, vol. 67, no. 2, pp. 969–979, Feb. 2020, doi: 10.1109/TIE.2019.2901636.

[17] J. J. Aciego, I. González Prieto, M. J. Duran, M. Bermudez, and P. Salas-Biedma, "Model Predictive Control Based on Dynamic Voltage Vectors for Six-Phase Induction Machines," *IEEE J. Emerg. Sel. Top. Power Electron.*, vol. 9, no. 3, pp. 2710–2722, Jun. 2021, doi: 10.1109/JESTPE.2020.2977144.

[18] W. Song, M. S. R. Saeed, B. Yu, J. Li, and Y. Guo, "Model Predictive Current Control with Reduced Complexity for Five-Phase Three-Level NPC Voltage-Source Inverters," *IEEE Trans. Transp. Electrification*, pp. 1–1, 2021, doi: 10.1109/TTE.2021.3131420.

[19] P. F. C. Gonçalves, S. M. A. Cruz, and A. M. S. Mendes, "Multistage Predictive Current Control Based on Virtual Vectors for the Reduction of Current Harmonics in Six-Phase PMSMs," *IEEE Trans. Energy Convers.*, vol. 36, no. 2, pp. 1368–1377, Jun. 2021, doi: 10.1109/TEC.2021.3055340.

[20] M. Bermúdez, C. Martín, F. Barrero, and X. Kestelyn, "Predictive controller considering electrical constraints: a case example for five-phase induction machines," *IET Electr. Power Appl.*, vol. 13, no. 8, pp. 1079–1088(9), Aug. 2019.

[21] M. Bermúdez, "Novel control techniques in multiphase drives: Direct control methods (DTC and MPC) under limit situations," *PhD Thesis*, l'École Nationale Supérieure d'Arts et Métiers ParisTech - Campus de Lille, 2018.

[22] Y. Wang and S. Boyd, "Fast Model Predictive Control Using Online Optimization," *IEEE Trans. Control Syst. Technol.*, vol. 18, no. 2, pp. 267–278, Mar. 2010, doi: 10.1109/TCST.2009.2017934.

[23] C. S. Lim, E. Levi, M. Jones, N. A. Rahim, and W.-P. Hew, "A Fault-Tolerant Two-Motor Drive With FCS-MP-Based Flux and Torque Control," *IEEE Trans. Ind. Electron.*, vol. 61, no. 12, pp. 6603–6614, Dec. 2014, doi: 10.1109/TIE.2014.2317135.

[24] Y. Zhao and T. A. Lipo, "Space vector PWM control of dual three-phase induction machine using vector space decomposition," *IEEE Trans. Ind. Appl.*, vol. 31, no. 5, pp. 1100–1109, Sep. 1995, doi: 10.1109/28.464525.

[25] W. Wu, Y. Liu, Y. He, H. S.-H. Chung, M. Liserre, and F. Blaabjerg, "Damping Methods for Resonances Caused by LCL-Filter-Based Current-Controlled Grid-Tied Power Inverters: An Overview," *IEEE Trans. Ind. Electron.*, vol. 64, no. 9, pp. 7402–7413, Sep. 2017, doi: 10.1109/TIE.2017.2714143.

[26] J. He, Y. W. Li, F. Blaabjerg, and X. Wang, "Active Harmonic Filtering Using Current-Controlled, Grid-Connected DG Units With Closed-Loop Power Control," *IEEE Trans. Power Electron.*, vol. 29, no. 2, pp. 642–653, Feb. 2014, doi: 10.1109/TPEL.2013.2255895.

[27] J. A. Rossiter, *Model-based predictive control: a practical approach*. Boca Raton: CRC Press, 2003.

[28] S. Bolognani, S. Bolognani, L. Peretti, and M. Zigliotto, "Design and Implementation of Model Predictive Control for Electrical Motor Drives," *IEEE Trans. Ind. Electron.*, vol. 56, no. 6, pp. 1925–1936, Jun. 2009, doi: 10.1109/TIE.2008.2007547.

[29] H. T. Nguyen and J.-W. Jung, "Disturbance-Rejection-Based Model Predictive Control: Flexible-Mode Design with a Modulator for Three-Phase Inverters," *IEEE Trans. Ind. Electron.*, vol. 65, no. 4, pp. 2893–2903, Apr. 2018, doi: 10.1109/TIE.2017.2758723.

[30] C. S. Lim, S. S. Lee, I. U. Nutkani, X. Kong, and H. H. Goh, "Near-Optimal MPC Algorithm for Actively Damped Grid-Connected PWM-VSCs With LCL Filters," *IEEE Trans. Ind. Electron.*, vol. 67, no. 6, pp. 4578–4589, Jun. 2020, doi: 10.1109/TIE.2019.2924872.

[31] C. S. Lim, H. H. Goh, and S. S. Lee, "Long-Prediction-Horizon Near-Optimal Model Predictive Grid Current Control for PWM-Driven VSIs With LCL Filters," *IEEE Trans. Power Electron.*, vol. 36, no. 2, pp. 2246–2257, Feb. 2021, doi: 10.1109/TPEL.2020.3011227.

[32] S. Paul and K. Basu, "A Three-Phase Inverter Based Overmodulation Strategy of Asymmetrical Six-Phase Induction Machine," *IEEE Trans. Power Electron.*, vol. 36, no. 5, pp. 5802–5817, May 2021, doi: 10.1109/TPEL.2020.3026816.

[33] R. Bojoi, A. Tenconi, F. Profumo, G. Griva, and D. Martinello, "Complete analysis and comparative study of digital modulation techniques for dual three-phase AC motor drives," in *2002 IEEE 33rd Annual IEEE Power Electronics Specialists Conference. Proceedings (Cat. No.02CH37289)*, Jun. 2002, vol. 2, pp. 851–857 vol.2. doi: 10.1109/PSEC.2002.1022560.

[34] A. S. Abdel-Khalik, R. A. Hamdy, A. M. Massoud, and S. Ahmed, "Low-Order Space Harmonic Modeling of Asymmetrical Six-Phase Induction Machines," *IEEE Access*, vol. 7, pp. 6866–6876, 2019, doi: 10.1109/ACCESS.2018.2889044.

Chee Shen Lim (SM'19) received the B.Eng. (Hons.) degree in electrical engineering from the University of Malaya, Kuala Lumpur, Malaysia, in 2009, and the joint-university PhD degrees in power electronics and drives from the university of Malaya, Kuala Lumpur, and Liverpool John Moores University, Liverpool, U.K., in 2013.

From 2013 to 2015, he was a Research Scientist with the Experimental Power Grid Centre, Agency for Science, Technology and Research, Singapore. From 2015 to 2021, he was an Assistant/Associate Professor of electrical and electronic engineering with the University of Southampton Malaysia Campus. He is currently an Associate Professor of electrical and electronic engineering with Xi'an Jiaotong-Liverpool University, China. Dr. Lim serves currently as an Associate Editor of the IET Electric Power Applications.

Sze Sing Lee (SM'18) received the B.Eng. (Hons.) and PhD degrees in electrical engineering from Universiti Sains Malaysia, Malaysia, in 2010 and 2013, respectively.

He is currently an Assistant Professor with Newcastle University, Singapore. From 2014 to 2019, he was a Lecturer/Assistant Professor with the University of Southampton Malaysia Campus. From 2018 to 2019, he was a Visiting Research Professor with Ajou University, South Korea. Dr. Lee was a recipient of the Outstanding Reviewer Award from the IEEE Transactions on Power Electronics in 2020. He is an Associate Editor for the IEEE Trans. on Industrial Electronics and IEEE Access.

Emil Levi (S'89, M'92, SM'99, F'09) received his MSc and the PhD degrees in Electrical Engineering from the University of Belgrade, Yugoslavia in 1986 and 1990, respectively. He joined Liverpool John Moores University, UK in May 1992 and is since September 2000 Professor of Electric Machines and Drives. He served as a Co-Editor-in-Chief of the IEEE Trans. on Industrial Electronics in the 2009-2013 period. Currently he is Editor-in-Chief of the IEEE Trans. on Industrial Electronics and Editor-in-Chief of the IET Electric Power Applications. He is the recipient of the Cyril Veinott award of the IEEE Power and Energy Society for 2009 and the Best Paper award of the IEEE Trans. on Industrial Electronics for 2008. In 2014 he received the "Outstanding Achievement Award" from the European Power Electronics (EPE) Association and in 2018 the "Professor Istvan Nagy Award" from the Power Electronics and Motion Control (PEMC) Council.